AGU PUBLICATIONS

JGR

Journal of Geophysical Research: Solid Earth

RESEARCH ARTICLE
10.1002/2017JB015198

Key Points:
- Detailed study of waveforms from seismic activity at the İzmit-Düzce rupture zone in NW Turkey is presented
- New advanced waveform processing results in the detection of prominent secondary phases in *P* wave coda well separated from direct *P* wave
- Polarization analysis reveals *PS* phase converted at the upper crustal structure in agreement with near-fault setting of the Mudurnu segment

Supporting Information:
- Supporting Information S1

Correspondence to:
P. Hrubcová,
pavla@ig.cas.cz

Citation:
Najdahmadi, B., Hrubcová, P., Vavryčuk, V., & Bohnhoff, M. (2018). Imaging the Mudurnu segment of the North Anatolian Fault Zone from waveforms of small earthquakes. *Journal of Geophysical Research: Solid Earth*, *123*, 493–512. https://doi.org/10.1002/2017JB015198

Received 7 NOV 2017
Accepted 20 DEC 2017
Accepted article online 28 DEC 2017
Published online 22 JAN 2018

Imaging the Mudurnu Segment of the North Anatolian Fault Zone From Waveforms of Small Earthquakes

Bita Najdahmadi[1], Pavla Hrubcová[2], Václav Vavryčuk[2], and Marco Bohnhoff[1,3]

[1]Section 4.2: Geomechanics and Rheology, Helmholtz-Centre Potsdam, GFZ German Centre for Geosciences, Potsdam, Germany, [2]Institute of Geophysics, Czech Academy of Sciences, Prague, Czech Republic, [3]Institute of Geological Sciences, Free University Berlin, Berlin, Germany

Abstract We analyze waveforms of local earthquakes occurring before, between, and after the two consecutive 1999 $M_w > 7$ İzmit and Düzce earthquakes in NW Turkey. The waveforms were recorded at three seismic stations DOK, EKI, and GOK located around the Mudurnu segment of the North Anatolian Fault Zone. We focus on the interpretation of a distinct secondary phase contained in the *P* wave coda that is well separated from the direct *P* wave. The phase is visible in many waveforms of most seismicity clusters and has a specific constant time delay after the direct *P* wave arrivals at each station, irrespective of epicentral distance, hypocentral depth, or back azimuth. Based on a polarization analysis of records at station GOK, this secondary phase is interpreted as a *PS* wave converted at an interface near the stations. Its particle motion is consistent with the direct *S* wave and displays *S* wave splitting produced by the anisotropic upper crust. Synthetic modeling indicates that this *PS* phase can be converted either at a horizontal interface or at a steeply inclined interface. The steep Mudurnu fault zone with the near-surface setting indicating a juvenile pull-apart structure fits well into these interpretations, which are in agreement with the eastward progressing transtensional tectonics known for the region.

1. Introduction

An identification of down-dip extension of faults and detailed structure of the upper crust is key issue in imaging locations and geometries of future earthquake ruptures. Active wide aperture and multichannel seismic profiling can provide such information but require substantial budgets for data acquisition. However, both cannot image near-vertical fault planes (e.g., Brückl et al., 2007; Kaiser et al., 2009; Thybo et al., 2003; Yang, 2015). These difficulties can be overcome by studying local seismicity. Local earthquakes generate high-frequency seismic waves, which can be reflected and/or converted at structural horizontal or inclined interfaces or faults representing a first-order discontinuity with a velocity contrast. Consequently, waveforms of earthquakes recorded at local seismic networks can provide information that can be utilized for imaging the velocity structure (e.g., Eberhart-Phillips & Michael, 1993; Sanford et al., 1973; Wu & Lees, 1999) and the interfaces at depths. To perform this analysis, a novel concept for extracting crustal structure from high-frequency waveforms of local earthquakes was developed by Hrubcová et al. (2013, 2016) and applied for determining depth and topography of crustal discontinuities. The method has been tested on two local seismic data sets allowing for imaging horizontal interfaces at the site of the Continental Super-Deep Drilling Project (KTB) in Germany and in the West Bohemia earthquake swarm region in the Czech Republic.

In this paper, we extend the technique of Hrubcová et al. (2013, 2016) to near-fault zone seismic recordings along the North Anatolian Fault Zone (NAFZ) in northwestern Turkey with the aim to image the structure around the strike-slip Mudurnu segment as a major NAFZ branch. We use local seismicity in the period of 1997–2001 during which the two consecutive 1999 $M_w > 7$ İzmit and Düzce earthquakes occurred (e.g., Gülen et al., 2002; Tibi et al., 2001) (Figure 1). The data provide a unique opportunity to study source processes in the focal zone (e.g., Li et al., 2002; Örgülü & Aktar, 2001; Stierle, Vavryčuk, et al., 2014; Stierle, Bohnhoff, & Vavryčuk, 2014), local seismotectonic features (Bohnhoff et al., 2006; Bohnhoff, Ickrath, et al., 2016; Bulut et al., 2007), and structural characteristics of the Mudurnu area (e.g., Beyhan & Alkan, 2015; Bulut, Ben-Zion, et al., 2012; Görgün et al., 2010). A detailed analysis of waveforms enabled us to identify distinct secondary phases in the *P* wave coda at near-fault stations and to invert them for imaging sedimentary and upper crustal structure near the Mudurnu fault.

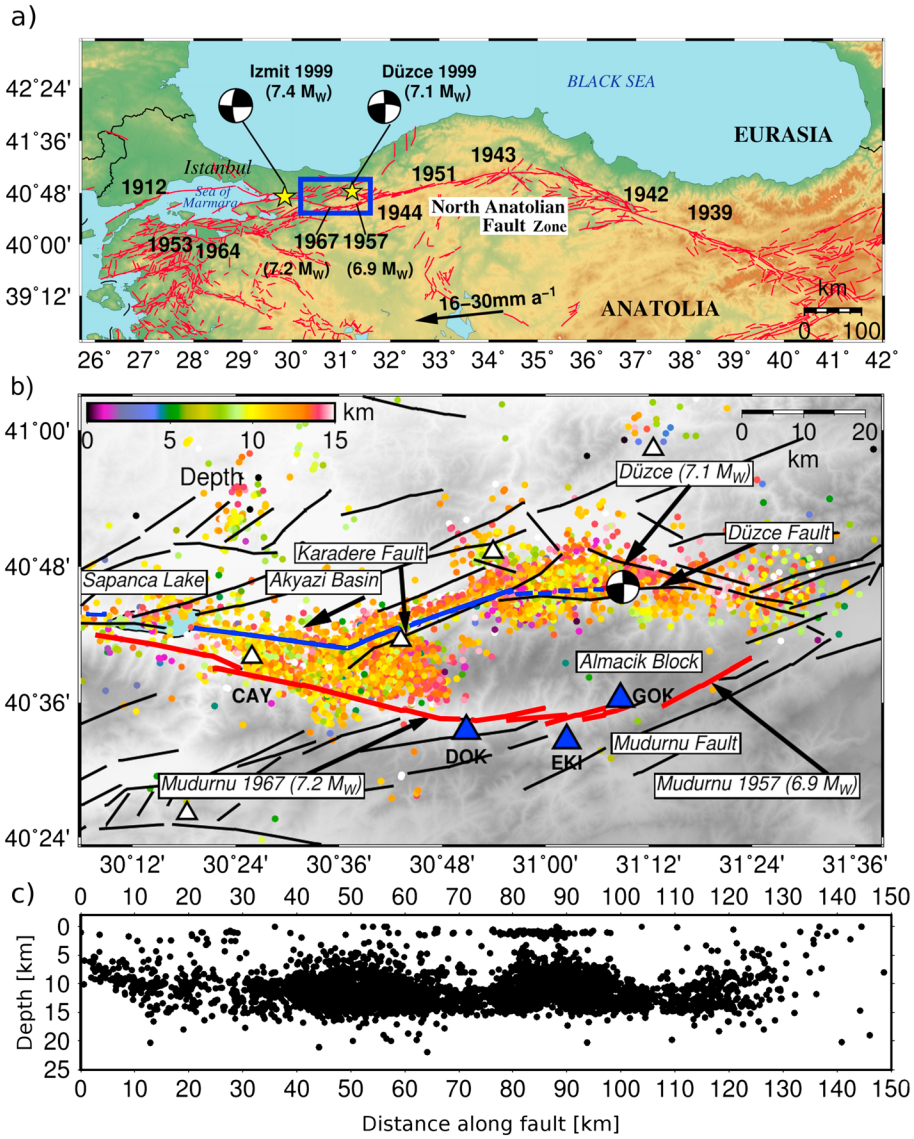

Figure 1. (a) Regional tectonic setting of the northern Anatolian region with the North Anatolian Fault Zone (NAFZ) as the right-lateral transform plate boundary between Anatolia and Eurasia. The black arrow indicates the present GPS-derived average right-lateral slip along the NAFZ (after McClusky et al., 2000). The black numbers show the locations of the $M_w > 6.9$ earthquakes during the twentieth century; note their westward migration with time. The 1999 İzmit and Düzce earthquakes are marked by yellow stars with corresponding focal mechanisms (after Özalaybey et al., 2002). The blue rectangle indicates the study area. (b) Study area with the Mudurnu fault (bold red line) as a major NAFZ branch that hosted large earthquakes in 1957 (M_w 6.9) and 1967 (M_w 7.1). The 1999 İzmit (blue line) and Düzce (dashed blue line) ruptures are indicated (after Barka et al., 2002). Additional NAFZ branches and nearby mapped faults are plotted by black lines. The white triangles mark seismic stations of the SABONET network (Milkereit et al., 2000); the blue triangles stand for three SABONET stations used in this study. The seismicity represents catalogue events from 1997 to 2001 as recorded at stations DOK, EKI, and GOK (after Bohnhoff, Ickrath, et al., 2016) and is color-coded according to the hypocentral depth. The focal mechanism shows the epicenter and faulting mechanism of the Düzce earthquake. (c) Hypocentral depths of seismicity along the NAFZ section shown in Figure 1b.

2. Study Area and Data

2.1. Study Area

The North Anatolian Fault Zone is one of the largest plate-bounding transform faults separating the Anatolian and Eurasian Plates. Located in NW Turkey, it trends approximately east-west along a 1,300 km boundary between the Eastern Anatolia and the Northern Aegean (e.g., Bohnhoff, Martínez-Garzón, et al., 2016;

Sengör et al., 2005). The westward movement of Anatolia is a result of the northward moving Arabian plate and the southward rollback of the Hellenic Subduction Zone where the African lithosphere is subducted below the Aegean (e.g., Bohnhoff, Harjes, & Meier, 2005; Bulut, Bohnhoff, et al., 2012; Flerit et al., 2004). The current right-lateral slip rate along the NAFZ is 16–30 mm/yr (e.g., Barka, 1992; McClusky et al., 2000), repeatedly producing major ($M_w > 7$) strike-slip earthquakes. During the twentieth century, the NAFZ has ruptured over 900 km of its length (Ambraseys & Zatopek, 1969; Barka et al., 2002) with a series of large earthquakes migrating generally westward toward the Istanbul-Marmara region in NW Turkey. The most recent $M_w > 7$ earthquakes in the NAFZ occurred in 1999: the M_w 7.4 İzmit earthquake and the M_w 7.1 Düzce earthquake (Figure 1) (e.g., Bohnhoff, Ickrath, et al., 2016; Tibi et al., 2001). They occurred in a place where the NAFZ splays into two branches: the Karadere-Düzce fault in the north and the Mudurnu fault in the south, with the Paleozoic-Eocene rocks of the Almacik block in-between (Figure 1b). The Mudurnu segment of the NAFZ connects with the Karadere fault below the Akyazi pull-apart basin in the west and the Düzce fault in the east. It represents the southern boundary of the uplifted crustal Almacik block and ruptured most recently during the 1957 M_w 6.9 and the 1967 M_w 7.1 earthquakes (Ambraseys & Zatopek, 1969).

In our study, we analyze waveform recordings of three seismic stations DOK, EKI, and GOK located around the Mudurnu segment of the NAFZ (Figure 1b). The stations are close to the fault; however, their local geology differs. Station GOK is surrounded by Devonian rocks and Upper Cretaceous flysch, which exist at the northern side of the fault and the block that has been affected by Caledonian and Hercynian orogenic movements. To the south, much younger rocks border the zone, the oldest of them being of Jurassic age. Station EKI is located in Jurassic rocks, mostly volcanic tuff series which lie unconformably on the crystalline series. Station DOK is surrounded by the intrusives (granites, syenites, diorites, pyroxenes, and serpentines) of the fault zone. To the south of the Mudurnu fault, Lower Cretaceous limestones occur, while north of stations DOK and EKI the metamorphic rocks and serpentines of the Almacik block are present (Ambraseys & Zatopek, 1969).

2.2. Previous Investigations

The Karadere-Düzce and Mudurnu faults are major NAFZ strands separated by Paleozoic-Eocene rocks of the elevated crustal Almacik block. Based on teleseismic tomography, this block was identified as a high-velocity body down to the base of the crust (Papaleo et al., 2017). Velocity contrasts across the Karadere fault and west of the Mudurnu fault were studied by fault zone head waves. Applying this approach, Najdahmadi et al. (2016) found a deep bimaterial interface with a velocity contrast of 3.4% down to the base of seismogenic crust and a shallow local bimaterial interface bounding a low-velocity damage zone or basin that extends to depths of 4–5 km below the Karadere fault. According to Dor et al. (2008), the Almacik block has faster seismic velocities at depth compared to both surrounding blocks. Thus, the southern branch of the NAFZ along the Almacik block (the Mudurnu fault) separates a high-velocity material in the north from slow-velocity material in the south, and vice versa for the northern branch (the Karadere-Düzce fault). Bulut, Ben-Zion, et al. (2012) disclosed a velocity contrast of ~6% across the western Mudurnu fault close to the station CAY (see Figure 1). The 3-D velocity model from local tomography detected higher V_p velocities between 4.4–6 km s^{-1} at depths of 0–10 km and ~6.5 km s^{-1} at depths of 10–20 km (Beyhan & Alkan, 2015).

The shear-wave splitting analysis of aftershocks following the 1999 M_w 7.4 İzmit earthquake enabled to delineate stress- and structure-controlled anisotropy in the upper crust along the western NAFZ (Eken et al., 2013; Hurd & Bohnhoff, 2012). Dominant fast shear-wave polarization trending NW-SE is parallel or subparallel with the strike of the regional maximum horizontal compressive stress and suggests a stress-controlled anisotropy in the study area. At some places, structure-controlled anisotropy was determined as possibly related to aligned macroscopic features associated with the Mudurnu fault (Hurd & Bohnhoff, 2012).

The moment tensors and focal mechanisms of aftershocks of the 1999 İzmit earthquake were studied by Stierle, Vavryčuk, et al. (2014) and Stierle, Bohnhoff, and Vavryčuk (2014). Though the events located in the Karadere-Düzce segment displayed significant differences in focal mechanisms, they exhibited only a small percentage of non-DC components in moment tensors, which, if existed, were mainly positive and deceased with time after the main shock indicating a crustal healing process (Stierle, Bohnhoff, et al., 2014). These results correlated well with the predominant strike-slip stress regime along the Karadere-Düzce segment and also with the main shock rupture being right-lateral strike-slip and temporarily introducing a dominantly normal-faulting regime (Bohnhoff et al., 2006; Ickrath et al., 2014, 2015). This is also in agreement with the

fault plane solutions of Örgülü and Aktar (2001) reflecting the complex source processes of the 17 August 1999 İzmit earthquake and local variations in the seismotectonic setting (Li et al., 2002).

2.3. Data

In this study, we use data from the seismic network SABONET (SApanca-BOlu NETwork), which consists of 15 stations equipped with short-period seismometers of type MARK L4-3D, with a natural frequency of 1 Hz and sampled at a rate of 100 Hz (Bindi et al., 2007; Ickrath et al., 2015; Milkereit et al., 2000). The seismicity studied here covers a 5 year (1997–2001) time window framing the two 1999 $M_w > 7$ İzmit and Düzce earthquakes and consists of absolute and relocated seismic events (Bohnhoff, Ickrath, et al., 2016; Ickrath et al., 2015). The majority of events occurred between depths of 6 and 16 km with only a small subset of events being located near the surface (Figure 1).

The SABONET hypocenter catalogue consists of absolute locations with an overall precision up to 3 km. Major part of the seismicity used in this study was relocated using the double-difference (hypoDD) earthquake relocation method of Waldhauser and Ellsworth (2000) with a final relative location accuracy of ~500 m (Bohnhoff, Ickrath, et al., 2016).

To image the Mudurnu segment, we selected earthquakes located along the İzmit-Düzce rupture zone north of the Almacik block recorded at three SABONET stations EKI, DOK, and GOK distributed around the Mudurnu fault south of the Almacik block (Figure 1b). Each of the stations recorded about 4,000 earthquakes with magnitudes in range of 0.9–3.8. In the analyzed seismograms, we manually revised *P* and *S* direct phase onset picks and performed several processing steps to detect and characterize secondary phases in the *P* wave coda.

3. Data Processing

In order to identify and systematically process the secondary phases in the *P* wave coda, the entire seismic data set of the earthquakes was divided into 45 spatially distributed clusters (see Figure S1a in the supporting information). The clusters were formed by earthquakes with similar epicenters (a typical diameter of such clusters is about 6 km) and cover the seismicity on both sides of the Karadere-Düzce fault from the west to the east. For each cluster, the waveforms were plotted with the aligned direct *P* wave arrivals and sorted according to their foci depths. The alignment according to direct *P* wave arrivals was further improved by the waveform cross correlation. Also, events with low signal-to-noise ratios were eliminated from the analysis. To enhance detection of secondary phases, the waveforms were filtered with a band-pass filter of 1–5 Hz and plotted depth-sorted with equidistant step in the seismic sections. After filtering, the low-frequency secondary phases became distinctly pronounced (see Figure S2 in the supporting information). Figure 2 shows the improvement in the secondary phase detection in the seismic section after the waveform processing with filtering, alignment, hypocentral-depth sorting, and equidistant plotting.

The waveform processing was performed for each individual cluster enabling us to detect the secondary phases generated by local crustal discontinuities and to enhance their visibility in the seismic sections. A systematic processing of seismic sections revealed the presence of coherent secondary phases coming in the *P* wave coda (Figure 2). The analysis showed that these phases are reasonably pronounced and separated from the direct *P* waves. Figures 3 and 4 present the examples of such phases at stations DOK, EKI, and GOK; details of the secondary phases for station GOK are summarized in Table S1 in the supporting information.

The presence of distinct secondary phases in records was checked manually cluster by cluster and the arrival times of the secondary phases were measured. Noteworthy, the time delay between the secondary phases identified in the records and the direct *P* arrivals did not change substantially within each cluster or among clusters at each station. However, the wavefields varied substantially among stations (see Figures 3 and 4). The recordings at stations DOK and EKI showed generally less pronounced and less consistent arrivals of the secondary phases than the recordings at station GOK. Also, the time delay of the arrival times between the direct *P* waves and the secondary phases varied among stations. Station DOK exhibited consistent onsets of secondary phases at 0.7 s after the *P* wave first arrival, some of the sections of the northern clusters showed also pronounced high-amplitude phases at 0.2 s after the *P* wave and high-amplitude phases before the *S* waves (see Figure 3a). Station EKI showed coherent secondary phases at 0.5 s, some clusters exhibited also

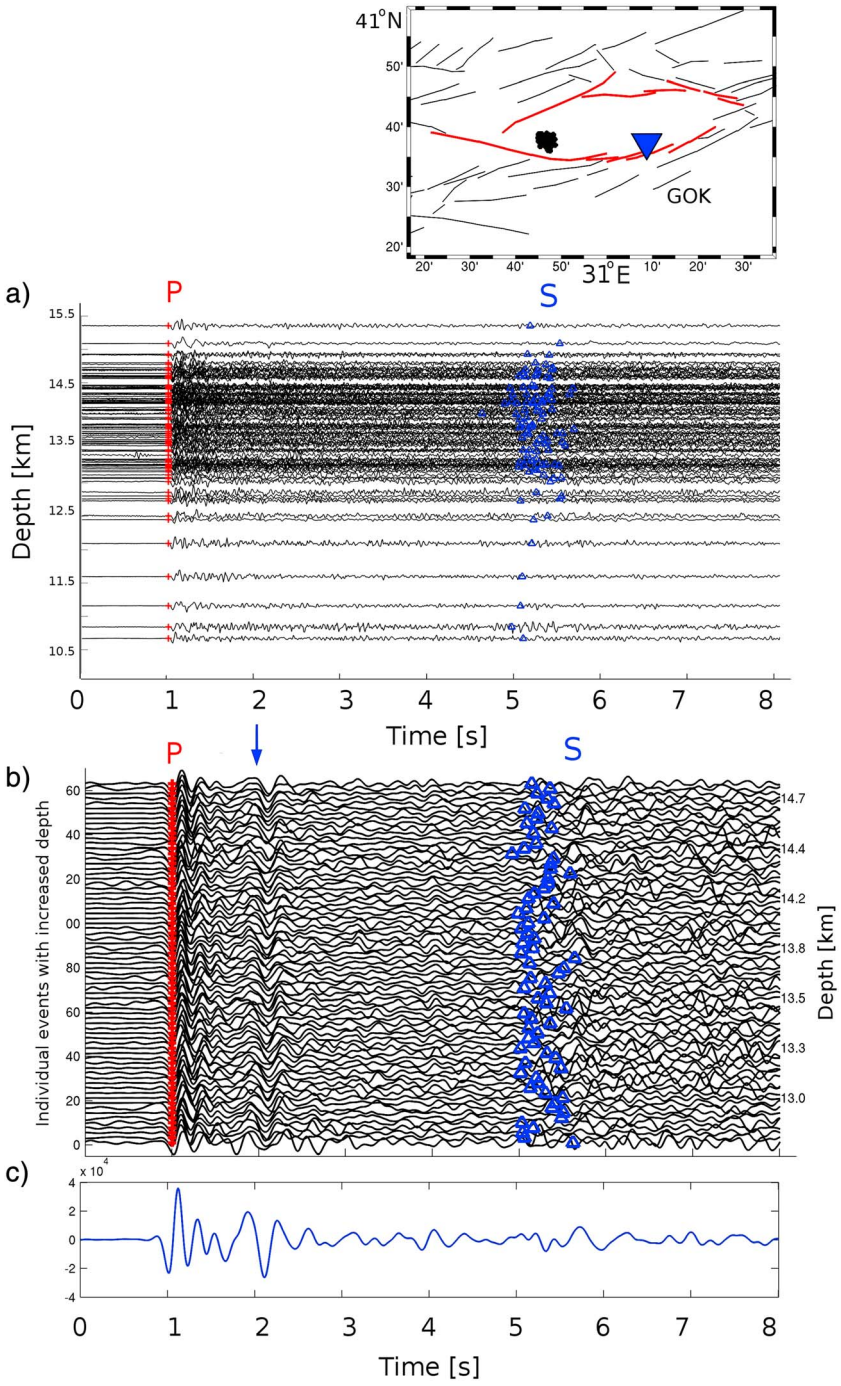

Figure 2. Waveform processing for enhancing detection of secondary phases in seismograms. (a) Unfiltered vertical component waveforms recorded at station GOK plotted with the *P* wave alignment according to increased hypocentral depth. (b) Vertical component waveforms band-pass-filtered with 1–5 Hz, sorted according to hypocentral depth, and plotted equidistantly. The seismicity cluster is marked in the insert by black dots; the Karadere-Düzce and Mudurnu faults are color-coded in red. *P* wave arrivals are marked by red crosses; *S* wave arrivals are marked by blue triangles. Clear and consistent arrivals of the secondary phases after the direct *P* wave are indicated by blue arrow. (c) The stacked seismogram. Note the improvement in the secondary phases' detection after the waveform processing with filtering, *P* wave alignment, hypocentral depth sorting, and equidistant plotting.

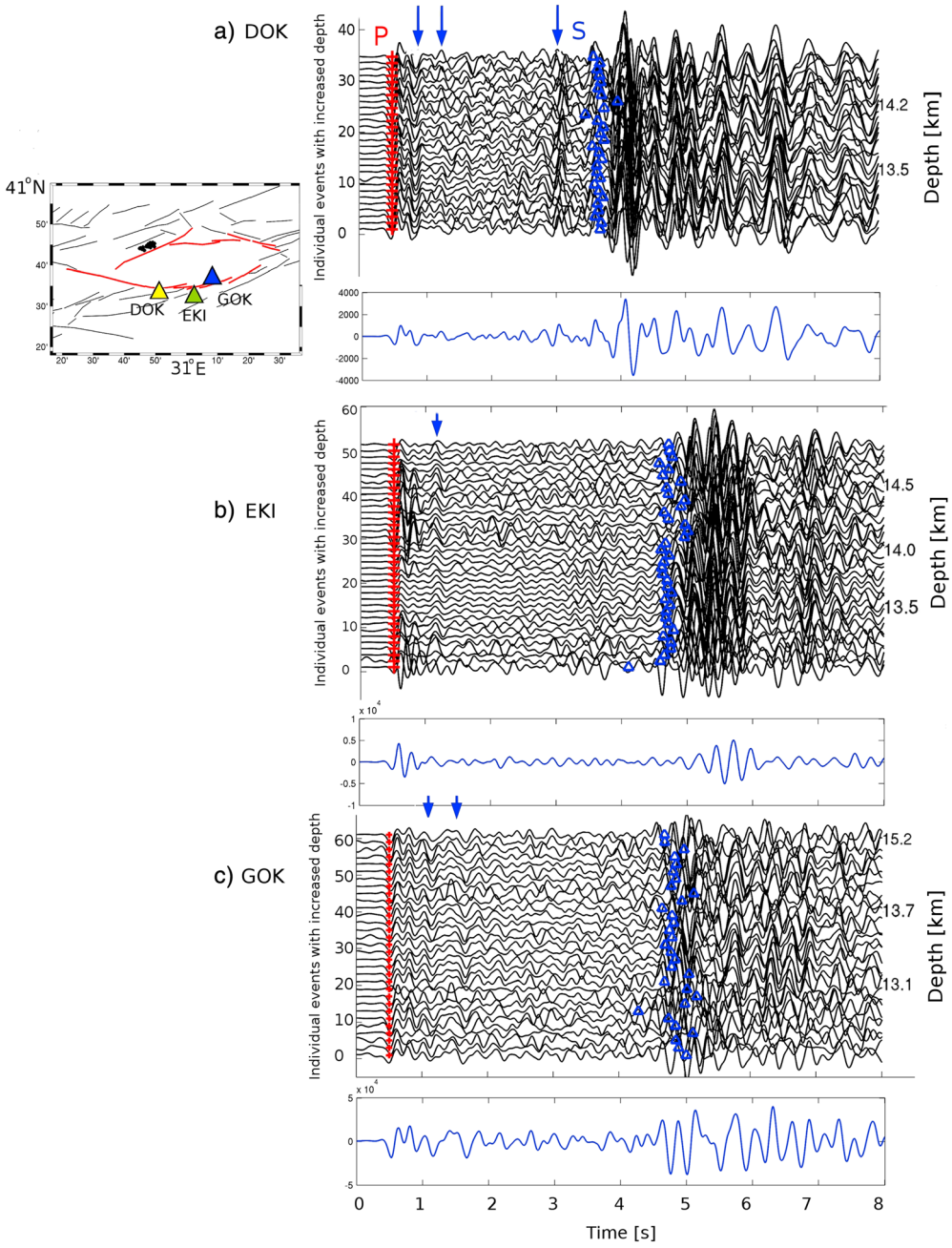

Figure 3. Vertical component seismic sections after the waveform processing for a seismic cluster in the north. Waveforms recorded at stations (a) DOK, (b) EKI, and (c) GOK. *P* wave arrivals are marked by red crosses; *S* wave arrivals are marked by blue triangles. The stacked seismograms are plotted below the waveforms for each station. The seismicity cluster is marked in the insert by black dots; the Karadere-Düzce and Mudurnu faults are color-coded in red. Note prominent secondary phases marked by blue arrows with the same time delay at each station and the variation in wavefields at different stations.

onsets at 0.2 s and 0.8 s (see Figures 3b and 4b). The time delay of the secondary phases at station GOK was 0.9 s (Figure 4c), some clusters also showed a preceding secondary phase at 0.5 s (Figure 3c).

The constant time delay of the secondary phases after the direct *P* wave arrivals and variations in the arrival times and amplitudes of the secondary phases among individual stations point to variations in local structure near the analyzed stations. Since station GOK showed high-quality recordings with the most consistent secondary phase well separated from the direct *P* wave at 0.9 s for most of the clusters, in further analysis, we

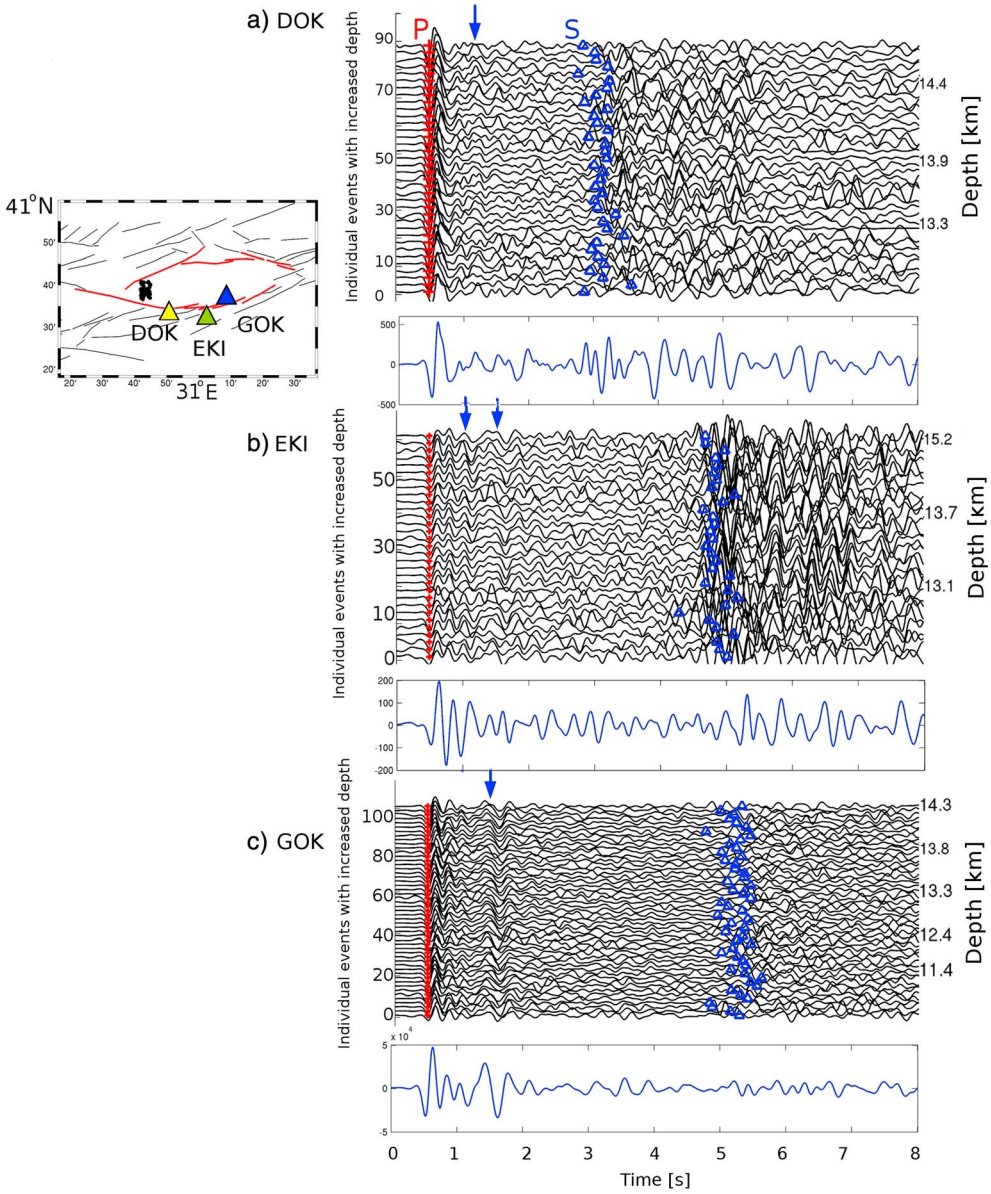

Figure 4. Vertical component seismic sections after the waveform processing of a seismicity cluster in the west marked in the insert. Waveforms recorded at stations (a) DOK, (b) EKI, and (c) GOK. The description as in Figure 3.

focused on this station and studied details in the time delay and type of this secondary phase. In the analysis of the time delays, we focused on the vertical components, since they showed clear and consistent onsets of secondary phase compared to the other components. The horizontal components were utilized in the analysis of particle motions aiming at differentiation of the phase type.

4. Data Analysis for Station GOK

4.1. Depth and Epicentral-Distance Sorting of Waveforms

First, we compared the time delays in depth-sorted sections of traces at station GOK for clusters with similar epicenters along the Karadere-Düzce fault (Figure 5). In order to enhance the visibility of the secondary phases and to avoid the effect of diversity of focal mechanisms and subsequent variations in the first-motion polarities in the recorded waveforms, we flipped some of the waveforms to get the same first-motion polarity in all vertical recordings in each cluster. This was applied mainly to the recordings of the northern and eastern

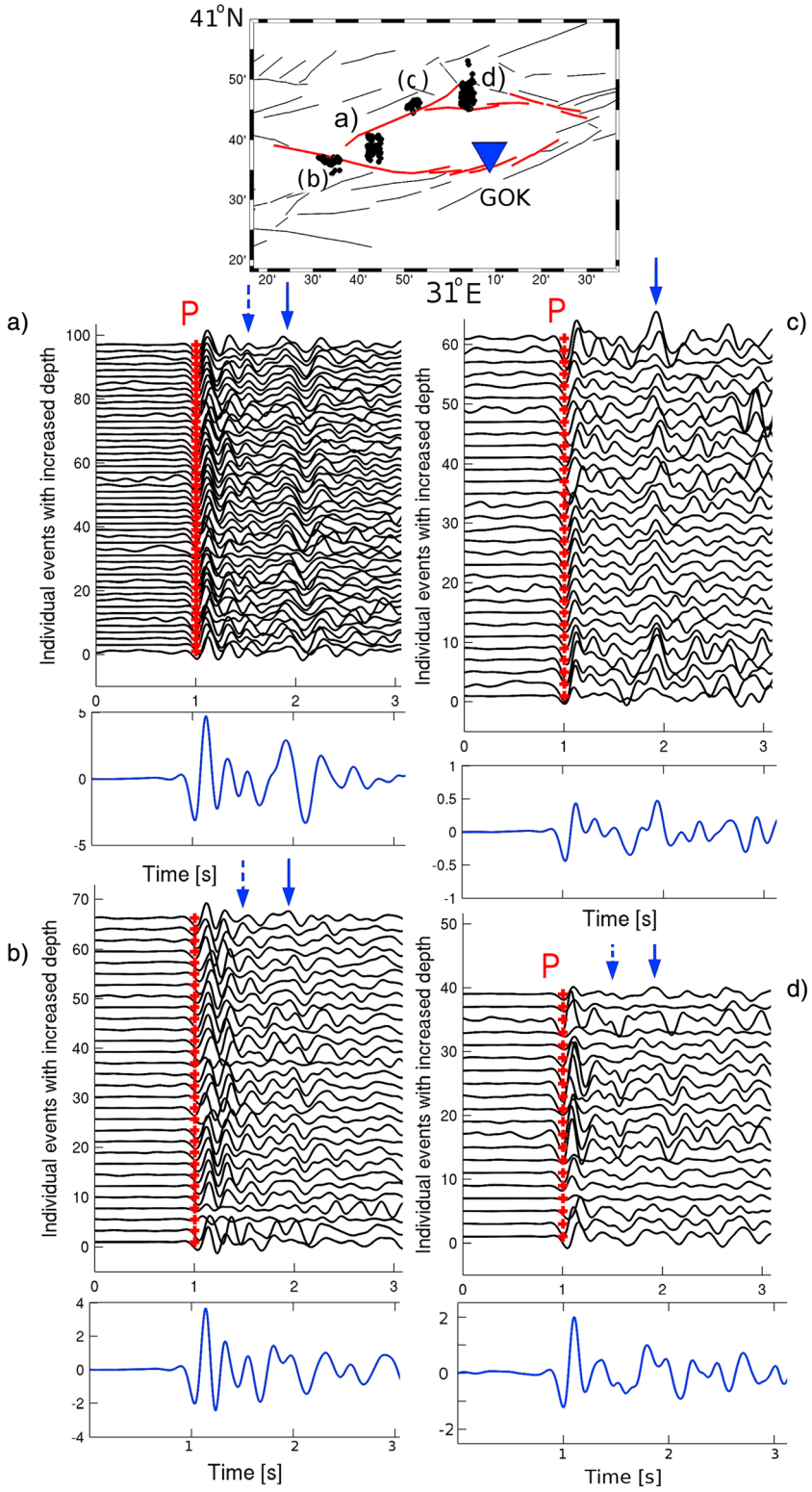

Figure 5. (a–d) Vertical component seismic sections after the waveform processing at station GOK at different azimuths. The stacked seismograms are presented beneath each seismic section. *P* wave arrivals are marked by red crosses; the blue arrows indicate the secondary phases (the solid blue arrow indicates the major secondary phase; the dashed blue arrow indicates the minor secondary phase). The seismicity clusters (Figures 5a–5d) are marked in the insert by black dots; the Karadere-Düzce and Mudurnu faults are color-coded in red. Note the same time delay of the respective secondary phases after the *P* waves for all clusters.

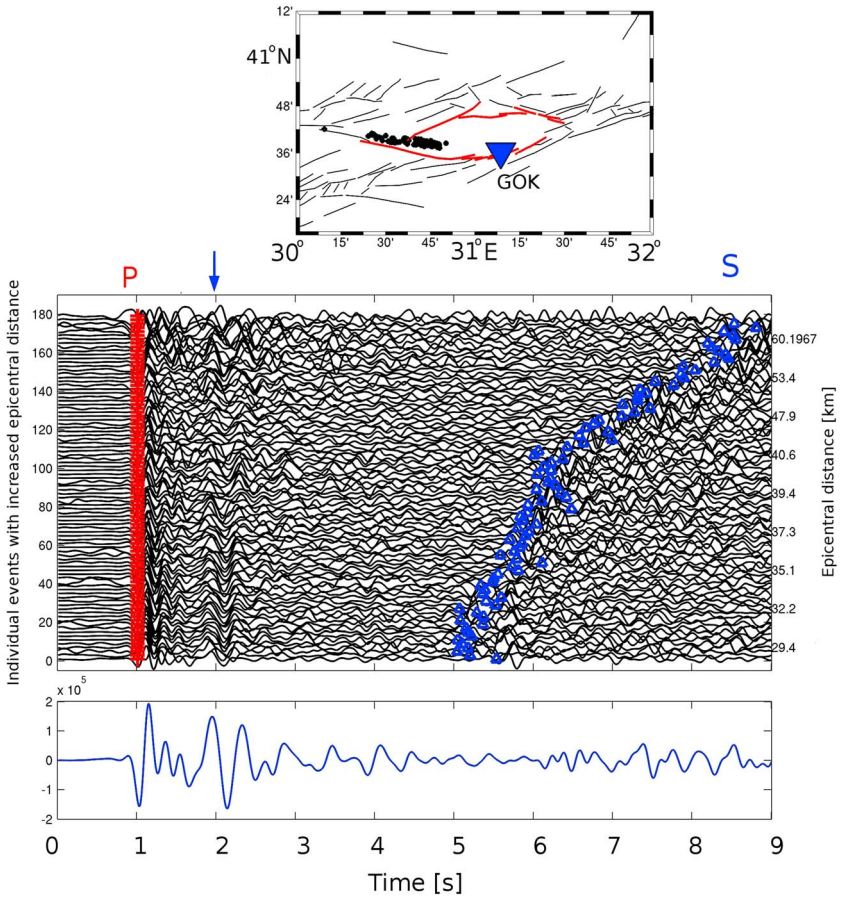

Figure 6. Vertical component seismic section after the waveform processing at station GOK plotted according to the increased epicentral distance (cluster 35 in Figure S1b in the supporting information). The stacked seismogram is presented beneath the section; note the comparable amplitudes of the secondary phase and the *P* wave. The seismicity cluster is marked in the insert by black dots; the Karadere-Düzce and Mudurnu faults are color-coded in red. *P* wave arrivals are marked by red crosses; *S* wave arrivals are marked by blue triangles; the blue arrow indicates the secondary phases. Note the consistent time delay of the secondary phases after the *P* waves despite the increase of epicentral distance.

clusters (see Table S1 in the supporting information), which resulted in an increased consistency of waveforms and in a better identification of the secondary phases in the seismic sections. As a result, a clear secondary phase appeared consistently in seismic sections of almost all clusters (see Figure 5). The time delay of this secondary phase (the major secondary phase) with respect to the direct *P* wave was the same disregarding the cluster locations and attained a value of 0.9 s. Some clusters also showed another preceding secondary phase at 0.5 s after the *P* wave (the minor secondary phase), though its amplitude was smaller and less consistent (Figure 5). Since this phase is too close to the direct *P* wave onsets and thus contaminated by the direct *P* wave, its detectability and resolution are lower. For these reasons, we mainly focus on the secondary phase at ~0.9 s after the *P* wave in further processing and interpretation.

Second, we sorted the waveforms according to the increased epicentral distance in order to confirm the constant time delay of ~0.9 s between the *P* wave and the secondary phase for other geometries. In this case, the seismicity was separated into 36 azimuthally variable segments covering the whole seismicity (see Figure S1b in the supporting information). For each segment, the waveforms were sorted according to epicentral distance in a narrow azimuthal range and plotted with the direct *P* wave alignment. Figure 6 shows an example of an epicentral-distance-sorted seismic section for one segment located in the west. The figure indicates that the section exhibits a constant time delay of the secondary phase with increasing epicentral distance, similarly as for the depth-sorted sections. A lower correlation of traces for the epicentral distances of ~40–50 km visible in Figure 6 (traces 100–130) evidences the transition of tectonic lines, the Mudurnu and

Karadere faults of the NAFZ. Such a setting produces more scattered waves, which is also visible in more reverberating waveforms along the whole raypath. Nevertheless, the presence of the secondary phase even in these waveforms, though less pronounced, documents a robust structure and represents another indication of the origin of secondary phase close to the station.

4.2. Quantitative Analysis of the Secondary Phases

The secondary phases exhibit a consistent time delay after the *P* wave in 32 clusters out of the original 45 spatially distributed clusters for depth sorting (see Table S1 in the supporting information). The consistence of the time delays was also confirmed for segments in epicentral-distance sorting. However, the character of the wavefield slightly differed for clusters from the west to the east. The secondary phases in the recordings from the western and northern clusters were more prominent compared to the recordings from the eastern clusters. Further to the east, the waveforms were nosier and less consistent within each cluster, which made the detection of the secondary phase more difficult. To assess the variations of the secondary phase in the waveforms for each cluster as well as among clusters quantitatively, we applied a waveform cross correlation. Figure 7a shows the distribution of the correlation coefficient for the secondary phases observed in the waveforms after processing. The correlation coefficient was calculated for a time window of 0.7–1.1 s after the direct *P* wave (the time window of the major phase) as the mean value for all events in each cluster and varied in a range of 0.35–0.82 (see Table S1 in the supporting information). The clusters in the north and west exhibit higher correlation coefficients; the clusters in the east show lower correlation. The distribution of seismicity is marked in Figure 7b with the events color-coded according to correlation threshold of 0.5.

Next, we calculated the covariance as a measure of the similarity of waveforms in each cluster and among clusters. Figure 8 shows the covariance of vertical-component waveforms for three different clusters: two depth-sorted clusters in the west and north and one epicentral-distance-sorted cluster in the west. Noteworthy, the covariance amplitude peak at 0.93 s is consistent for all these clusters and indicates the consistency of the secondary phases at the delay time of 0.93 s after the *P* wave. Reverse polarity of the covariance amplitude for cluster in the north (Figure 8b) is probably due to differences in radiation patterns and focal mechanisms among clusters and underlines the importance of flipping of the waveforms (see Table S1 in the supporting information). Nevertheless, the time of this peak is the same as for the other clusters. Thus, the observation of secondary phases in the seismic sections is consistent for different clusters and represents a robust feature. The variations of the wavefields can be attributed to variations in radiation patterns of the earthquakes and to lateral inhomogeneities in the area.

4.3. Particle Motions

We assume that the secondary phases in the *P* wave coda are generated by a subsurface structure. They can be of *P*- or *S*-type being reflected or converted at subsurface layers. The type of the phases can be identified using the polarization analysis of the 3-D particle motions. Therefore, in addition to analyzing seismic sections of vertical components of waveforms in each cluster, we included the horizontal components and analyzed the polarization of the *P*, *S*, and the secondary waves for all waveforms within each cluster (Figure 9). The polarization analysis was performed for time windows around the secondary phases and was checked quantitatively using a moving time window following the approach of Allam and Ben-Zion (2012) and Jurkevics (1988) (see Figures S3–S5 in the supporting information).

The *P* wave onsets are characterized by a nearly vertical polarization in the direction of back azimuths (Figure 9b). The *S* waves are polarized horizontally in the NW-SE direction (or perpendicularly to this direction), irrespective of the event-station back azimuth (Figure 9e) and are in agreement with the results of the shear-wave splitting analysis performed by Hurd and Bohnhoff (2012). Apart from the *P* and *S* wave onsets, we focused on the polarization of the most prominent major secondary phase at ~0.9 s after the *P* wave. The particle motions of this phase (Figures 9d and 9f in violet) exhibit a horizontal polarization in the NW-SE direction independent of the cluster locations being thus consistent with the directions of the shear-wave splitting observed in the area (Hurd & Bohnhoff, 2012; Peng & Ben-Zion, 2004). This indicates that the major secondary phase is the *S*-type phase being influenced by anisotropy of the upper crust. Therefore, the secondary phase is probably the *PS* phase converted at a shallow crustal structure.

In addition, we analyzed the lower amplitude and less visible minor secondary phase detected at 0.5 s after the *P* wave. The particle motion of this phase shows a near vertical polarization representing a *P*-type phase

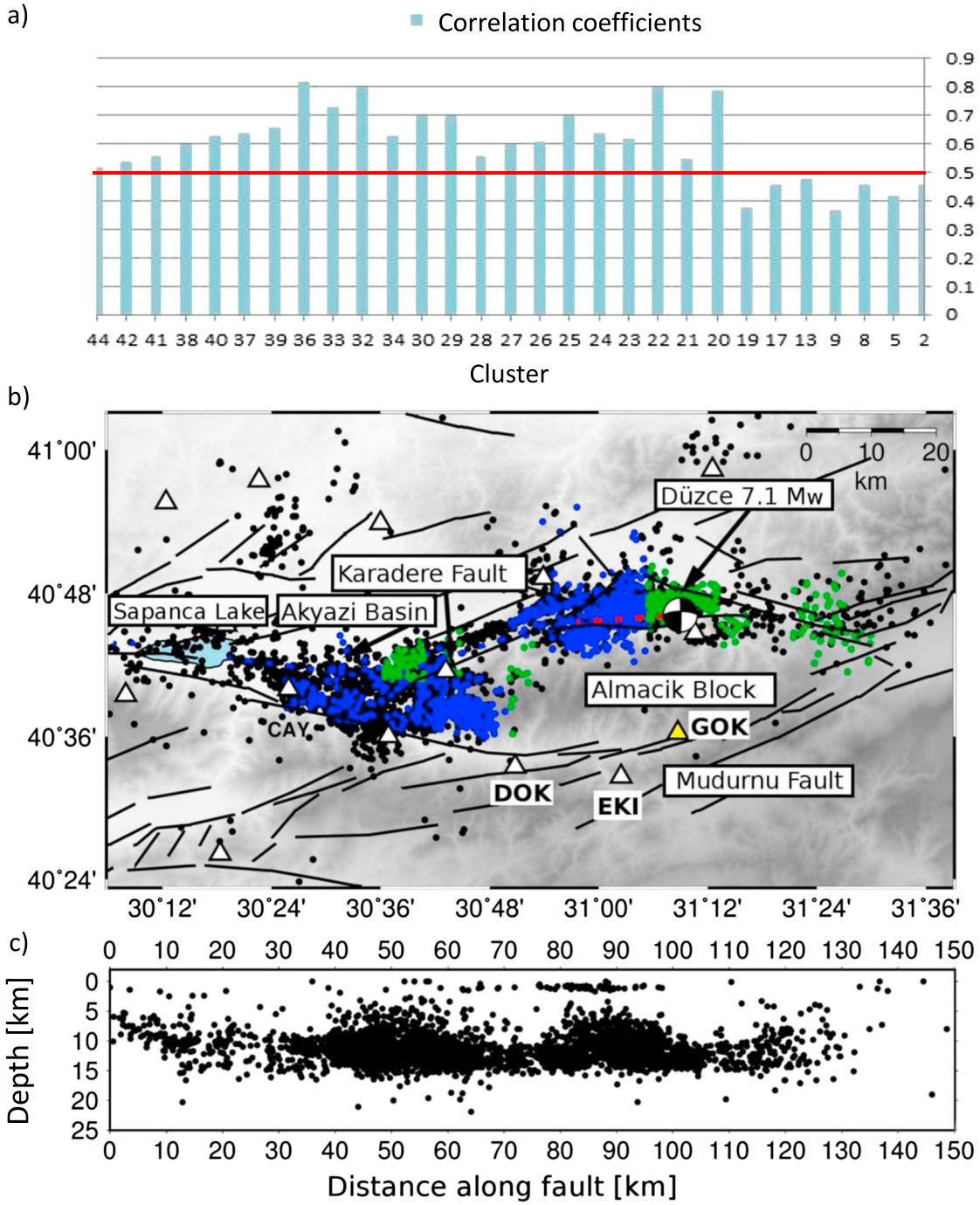

Figure 7. (a) Correlation coefficient of the secondary phases (the time window 0.7–1.1 s after the direct *P* arrival) for all analyzed clusters (see Figure S1a and Table S1 in the supporting information) at station GOK. Note lower correlation coefficients for clusters in the east (threshold of 0.5 marked by red line). (b) Seismicity along the Karadere-Düzce and partly Mudurnu faults with the events recorded at station GOK during 1997–2001. The events are color-coded according to the correlation coefficient of the secondary phases observed in the waveforms after processing: Seismic events with correlation coefficient $>$ 0.5 are marked in blue; seismic events with correlation coefficient $<$ 0.5 are marked in green. (c) Hypocentral depths of seismicity along the NAFZ section shown in Figure 7b.

(Figures 9c and 9f in red). Therefore, the *P*-type secondary phase can be either a *PPP* reflected wave generated by a shallow subsurface layer as discussed by Hrubcová et al. (2016) or a converted/reflected *PP* phase from an inclined interface. Variations in the incidence angle of the minor secondary phase and the direct *P* wave on the EW-NS plane for some clusters, however, indicate that the minor secondary phases are produced rather by reflections from a near-vertical structure (the Mudurnu fault zone).

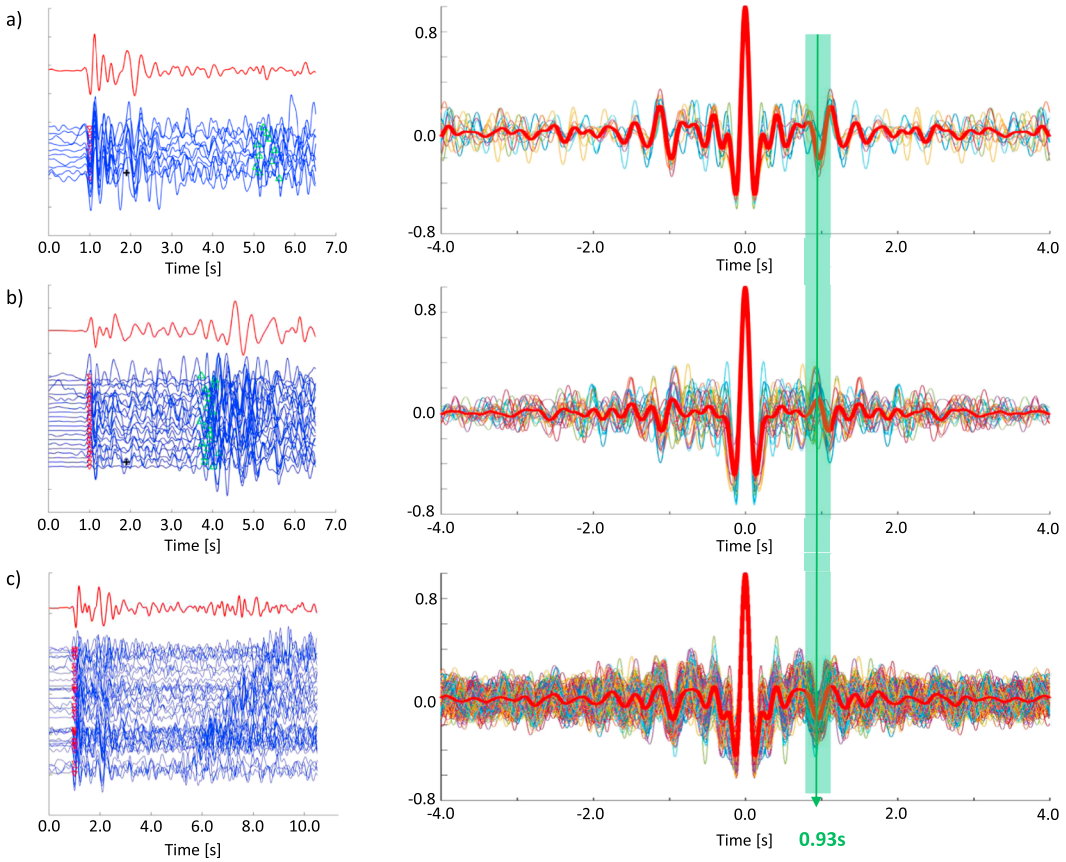

Figure 8. Examples of the covariance for three different clusters at station GOK: (a) depth-sorted cluster 32 in the west, (b) depth-sorted cluster 24 in the north, and (c) epicentral-distance-sorted cluster in the west (the same cluster as in Figure 6). (left column) Vertical component seismic sections after the waveform processing for each cluster, the stacked seismograms are plotted above the waveforms for each cluster in red. (right column) The covariance of waveforms in each cluster with the mean covariance marked in red. Note the covariance amplitude peak at 0.93 s (marked by green line) and the similarity in its wavelet (marked by green box) consistent for all clusters, which indicates the consistency of secondary phases at this time delay after the *P* wave. Reverse polarity of the covariance amplitude for cluster 24 is due to differences in radiation patterns and focal mechanisms among clusters and underlines the importance of flipping of the waveforms for enhancing their similarity.

The stability of particle motions of the analyzed phases is confirmed by the particle motion of the stacked phases (Figure 9f). It was also checked by polarization analysis with a moving time window in different clusters (Figures S3–S5 in the supporting information). The particle motion in the horizontal plane is close to the direction of the event-station back azimuth. The polarization of the minor secondary phase arriving at 0.5 s is also nearly vertical indicating that this phase is of the *P*-type. However, the polarization of this phase differs from the event-station back azimuth. This suggests that the waveforms are reflected from an interface. Later, as the major secondary phase arrives at the station, a clear change in the polarization is observed. The major secondary phase is mostly horizontal with azimuth consistent with the shear-wave splitting observed in the area (Hurd & Bohnhoff, 2012). Consequently, we conclude that the major secondary phase is of the *S*-type.

5. Synthetic Tests and Interpretation

Based on the low-frequency content and polarization, the major secondary phase is likely the *PS* conversion of the direct *P* wave. Since the time delay of this phase after the *P* wave does not change substantially with the epicentral distance of the analyzed clusters, the conversion point must be close to the station. To evidence the origin of such a *PS* phase, two possible scenarios were considered: (1) a near-horizontal converting interface and (2) a steeply inclined interface as a converting reflector. Both scenarios are plausible because the geological structure in the area, where the NAFZ is separated into the Mudurnu and Karadere-Düzce faults, is complicated. Both these faults delimit the crustal high-velocity Almacik block with velocities of

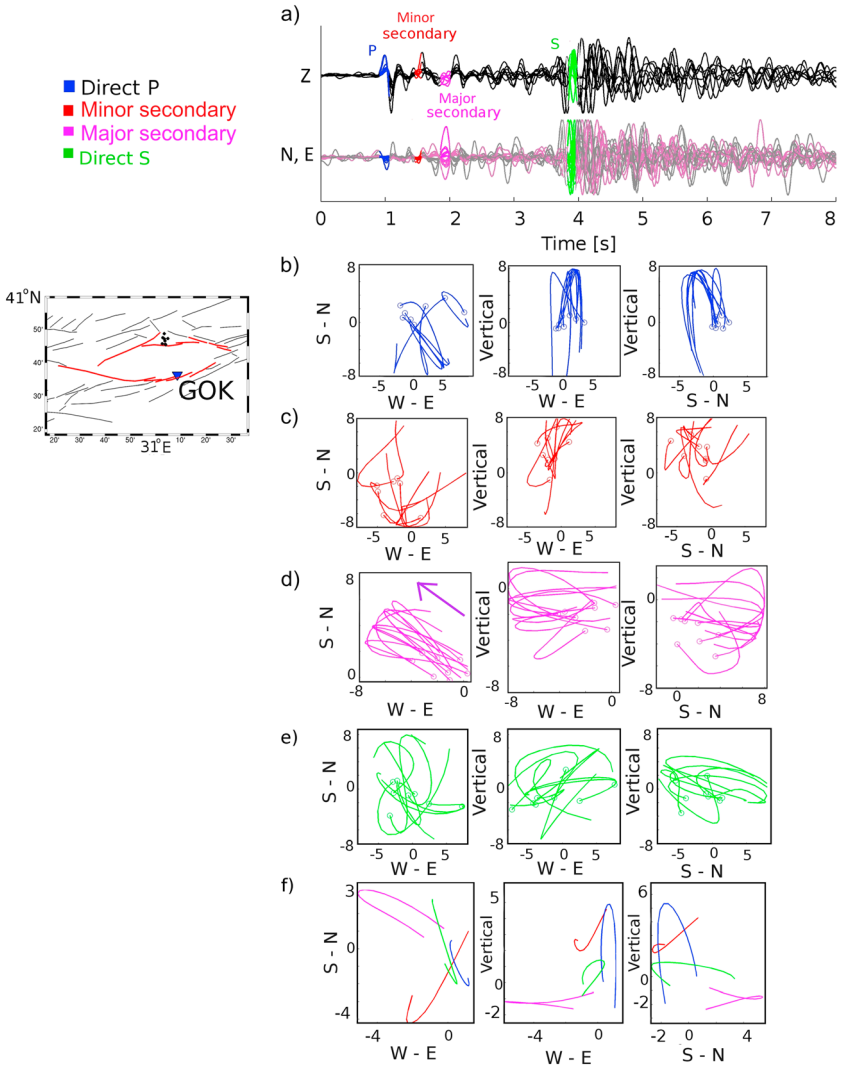

Figure 9. Particle motion analysis. (a) Three component waveforms recorded at station GOK. The seismicity cluster is marked in the insert by black dots; the Karadere-Düzce and Mudurnu faults are color-coded in red; the fast shear-wave polarization of the NW-SE direction is marked in Figure 9d by the violet arrow. The *P* waves (blue), major (violet), and minor (red) secondary phases are color-coded. (b–d) Particle motion plots for (b) the *P* wave, (c) minor, and (d) major secondary phases, (e) *S* wave, and (f) stacked phases in the EW-SN (left), EW-Z (middle), and SN-Z (right) projections with colors as in Figure 9a. Note the polarization of the major secondary phases (marked in violet) corresponding to the *S*-type phase being nearly horizontal in the vertical projections; its concordant direction with the fast shear-wave axis (marked by violet arrow in the EW-SN projection, after Hurd and Bohnhoff (2012)) indicates the influence by the anisotropy. The polarization of the minor secondary phase (marked in red) corresponds to the *P*-type phase being vertical or near vertical.

6 km s^{-1} surrounded by lower crustal velocities of 5 km s^{-1} as studied by Papaleo et al. (2017). To simulate the observed data, we applied real source-receiver geometry for station GOK, tested various focal mechanisms and simulated the sources of depth-sorted as well as epicentral-distance-sorted seismicity. Synthetic tests were performed for a simple velocity model consisted of two layers with velocities of 6 km s^{-1} simulating structures of the Almacik block and 5 km s^{-1} representing crustal velocities in its vicinity. The pronounced discontinuity with the velocity contrast of 1 km s^{-1} was assumed at varying depths; the goal was to find the optimum depth for which the *PS* phase is separated from the *P* wave with the observed time delay of ~0.9 s.

For the horizontal converting interface, the synthetic waveforms were calculated by the discrete wave number approach (Bouchon, 1981). Figure 10 documents the *PS* phase for 11 events located at a depth range of 10–15 km with a focal mechanism after Stierle, Bohnhoff, and Vavryčuk (2014) (their Table 3, mechanism 33) for one selected northern depth-sorted cluster. Figure 10a presents the velocity contrast with the downward

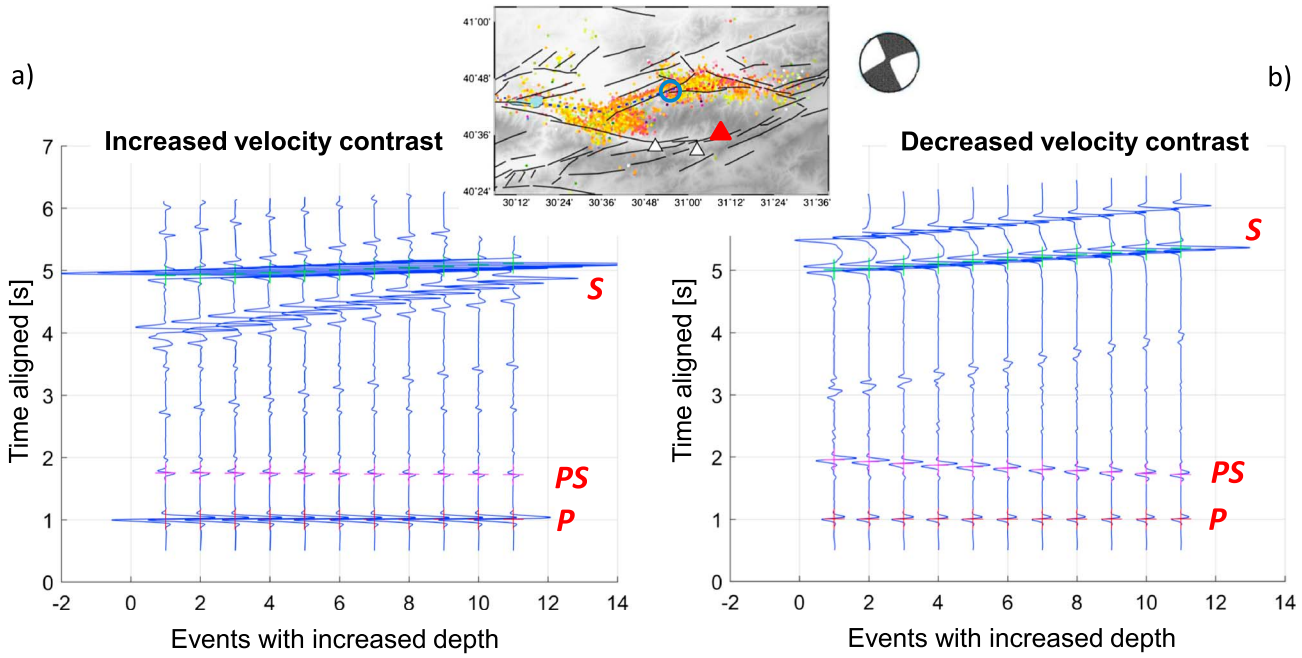

Figure 10. Vertical component synthetic sections for the depth-sorted seismicity (depths of 10–15 km) at station GOK for a model with one horizontal interface. The seismicity cluster in the north is indicated in the insert, the focal mechanism applied after Stierle, Bohnhoff, and Vavryčuk (2014) (their Table 3, mechanism 33, interpreted for this location), filtered 1–10 Hz. (a) Positive velocity contrast with the downward velocity increase from 5 to 6 km s^{-1} at a depth of 4 km. Note a constant time delay of the *PS* phase after the *P* wave. (b) Reverse velocity contrast with the downward velocity decrease from 6 to 5 km s^{-1} at a depth of 3 km. Note higher amplitude of the *PS* phase, though its time delay is not exactly constant.

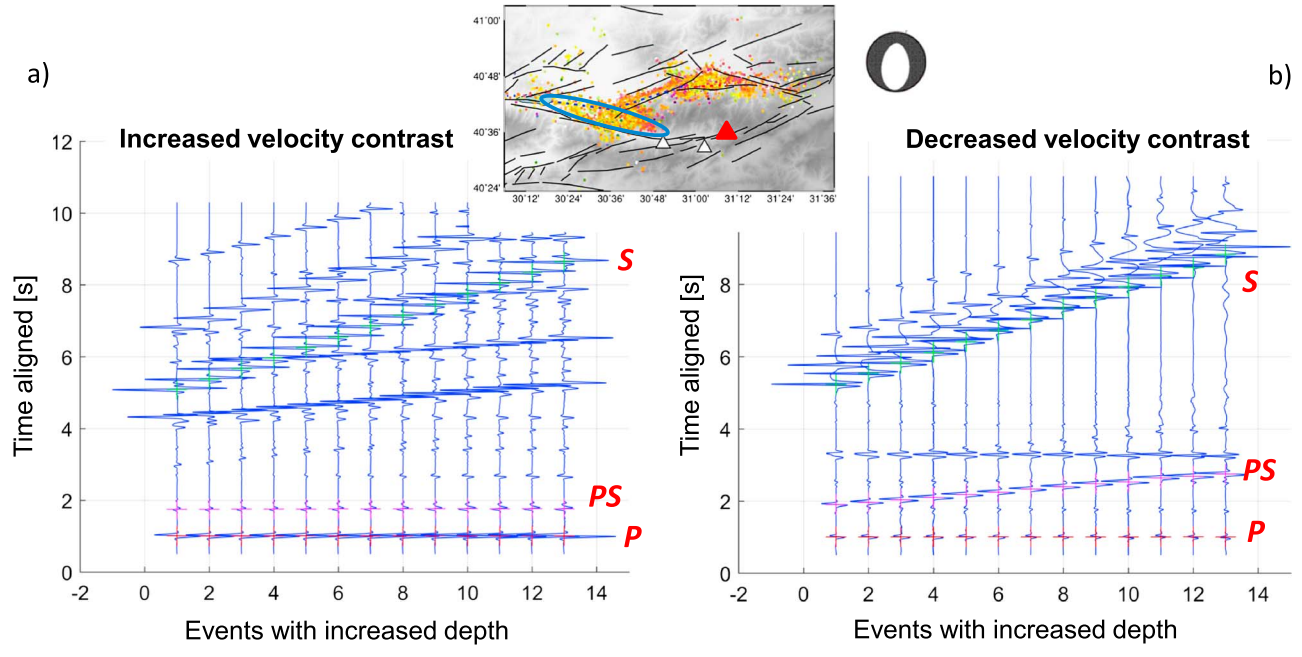

Figure 11. Vertical component synthetic section for the epicentral-distance-sorted seismicity at station GOK for a model with one horizontal interface. The seismicity cluster in the west is indicated in the insert, the depth of events is fixed at 11.5 km, the epicentral distances range between 30–60 km, the focal mechanism applied after Stierle, Bohnhoff, and Vavryčuk (2014) (their Table 3, mechanism 16, interpreted for this location), filtered with 1–10 Hz. (a) Positive velocity contrast with the downward velocity increase from 5 to 6 km s^{-1} at a depth of 4 km. Note constant time delay of the *PS* phase after the *P* wave. (b) Reverse velocity contrast with the downward velocity decrease from 6 to 5 km s^{-1} at a depth of 3 km. Note higher amplitude of the *PS* phase, though its time delay is not exactly constant.

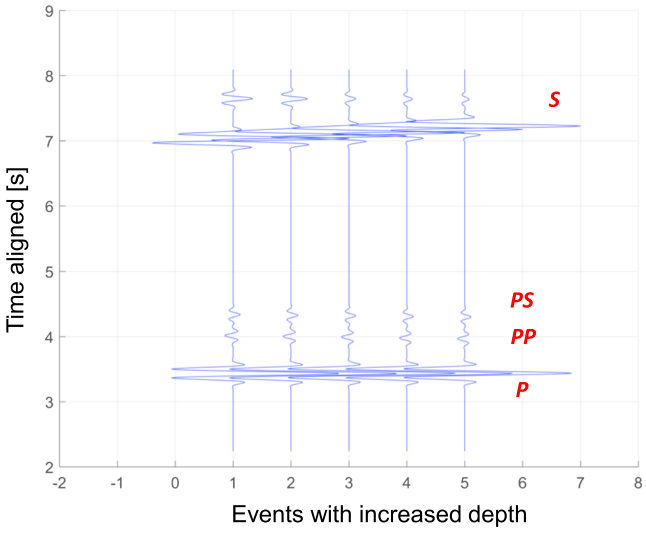

Figure 12. Vertical component synthetic section for the depth-sorted seismicity at station GOK for a model with an inclined interface. The seismicity cluster and focal mechanisms as in Figure 10; filtered 1–10 Hz. The velocity contrast is from 5 to 6 km s^{-1}. Note the constant time delay of the *PS* phase after the *P* wave together with the existence of preceding *PP* phase.

velocity increased from 5 to 6 km s^{-1} at a depth of 4 km. The *PS* phase is at 0.9 s after the *P* wave and exhibits a constant time delay for all events. Figure 10b shows a reverse velocity contrast with the downward velocity decreased from 6 to 5 km s^{-1} at a depth of 3 km. In this case, the *PS* phase is more pronounced; however, the *PS* arrival time after the *P* wave slightly varies with the depth of events.

To simulate the epicentral-distance-sorted seismic sections, we calculated synthetic waveforms for 13 events located at epicentral range of 30–60 km at a depth of 11.5 km; the focal mechanism was applied after Stierle, Bohnhoff, and Vavryčuk (2014) (their Table 3, mechanism 16). Figure 11a shows the results for the horizontal interface with a velocity contrast from velocity of 5 to 6 km s^{-1} at a depth of 4 km. As for the depth-sorted seismicity, the synthetic section exhibits constant time delay of the *PS* phase after the *P* wave, which agrees with the observed data. Figure 11b shows a reverse velocity contrast with the downward velocity decreased from 6 to 5 km s^{-1} at a depth of 3 km. In this case, the *PS* phase is more pronounced; however, the *PS* arrival time after the *P* wave slightly varies with the increasing epicentral distance of the events. The constant time delay of the secondary phase would be achieved for the *SP* converted phase or *PPP* phase reflected from the surface. However, such *P*-type phase is not in agreement with the particle motions of the secondary phase observed in the data.

For a steeply inclined interface, we simulated the Mudurnu fault zone located close to station GOK as the *PS* reflecting convertor. We tested the velocity contrast from 5 to 6 km s^{-1} on both sides of the interface and its inclination. The 2-D structure was modeled by using the ray-tracing program package SEIS83 (Červený & Pšenčík, 1984). The synthetic waveforms were calculated for events located at a depth range of 10.5–14.5 km simulating the same northern cluster as in the case of the model with the horizontal interface. The waveforms for a model with the inclined interface are more complex. The inclined interface produces not only the *PS* reflected conversions but also the *P*-to-*P* (*PP*) reflections from the same discontinuity. In addition, the tests show that the time delay of the *PS* phase is constant for both velocity contrasts (Figure 12). The *PS* amplitude depends on the incidence angle of the impinging rays at the interface, and it is rather small for steeply inclined interfaces. Also, the preceded *PP* reflection from the same interface has comparably small amplitudes. Less inclined interfaces produce critical and over-critical *PS* rays with higher amplitudes. In this case, the amplitudes of the *PP* reflections are also overcritical, and thus dominant in the waveforms. The impinging rays touch the interface at shallow depths of ~2–3 km.

To conclude, the synthetic tests for a model with a horizontal interface show a secondary *PS* phase with constant time delays of 0.9 s as observed in the data for both depth and epicentral-distance sorting with the positive (increasing) contrast from velocity of 5 to 6 km s^{-1} (Figures 10a and 11a). However, the model with the positive velocity contrast produces another phase arriving before the *S* wave, which is not observed in the data. The tests with the negative (decreasing) contrast from velocities of 6 to 5 km s^{-1} show a converted *PS* phase (Figures 10b and 11b); however, its arrival time after the *P* wave is not constant, which contradicts with the data. Thus, the synthetic tests indicate complicated setting in the area where the inclined interface represents the most probable interpretation of the origin of the *PS* secondary phase.

In synthetic modeling, we aimed at finding a plausible generator of the *PS* phase and its optimum depth/geometry for which this phase is separated from the *P* wave with the observed time delay of ~0.9 s. We aimed at key aspects producing such a phase taking into account following factors. (1) We simplified the structure into two layers with contrasting velocities detected in the region (Papaleo et al., 2017). (2) We did not attempt modeling of a low-velocity zone near the surface to avoid blurring the synthetic results by other minor phases. (3) We filtered the synthetic waveforms with the filter of 1–10 Hz to increase the resolution and highlight the onsets of individual phases. Since the data were filtered with 1–5 Hz, we provide comparison of the synthetics filtered with 1–10 Hz and 1–5 Hz in Figure S6 in the supporting information. (4) We did not apply the attenuation to keep high resolution of individual phases. (5) We tested different

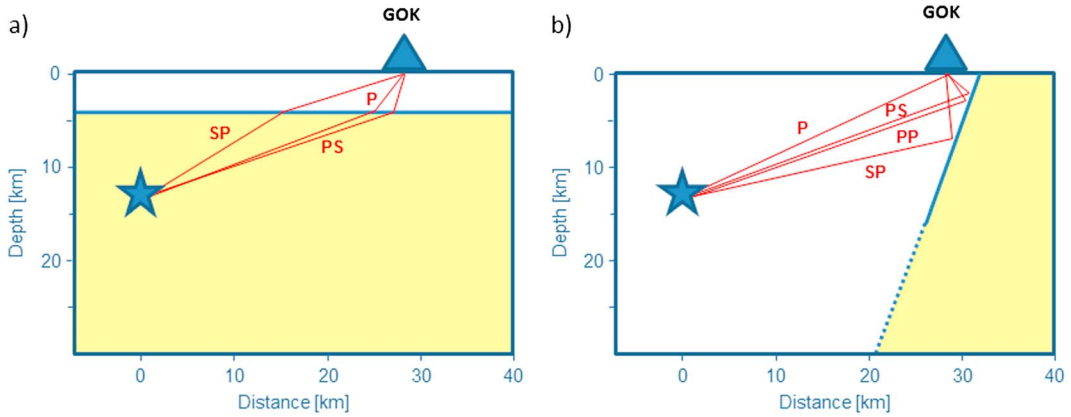

Figure 13. (a) Schematic sketch of a model with a horizontal interface producing the *PS* phase. (b) Schematic sketch of a model with a steeply inclined reflecting/converting interface (or fault zone) producing both major *PS* reflected conversions and minor *PP* reflections. The rays are indicated by red lines; the interfaces are indicated by blue lines.

mechanisms to see the dependency of waveforms on focal mechanisms (Figure S7 in the supporting information) and simulated shallow weathered layer as reported for many areas (e.g., Vavryčuk et al., 2004). (6) We aimed at fitting the time delays; we did not attempt to fit the amplitudes of the phases, since the amplitude ratio of the *P* wave and the secondary phase is strongly influenced by parameters of filtering (see Figure S2 in the supporting information).

6. Discussion and Conclusions

We analyzed about 4,000 earthquakes recorded at three stations of the SABONET network located around the Mudurnu segment of the NAFZ in the NW Turkey. The earthquakes are located along the İzmit-Düzce rupture zone of the NAFZ north of the Almacik block and are recorded at three SABONET stations EKI, DOK, and GOK (Figure 1). We focused on the interpretation of secondary phases contained in the *P* wave coda that are well separated from the direct *P* wave. The analyzed earthquakes were sorted into spatial clusters covering the entire seismically active zone. In order to reliably detect the secondary phases in the waveforms, the waveform processing consisted of the following steps:

1. Low-frequency band-pass filtering (1–5 Hz) to enhance the signal-to-noise ratio for the secondary phases.
2. *P* wave alignment of traces based on the waveform cross correlation.
3. Polarity flipping of some traces to obtain uniform *P* wave polarities at all traces and to suppress azimuthal dependence of body wave polarities due to focal mechanisms.
4. Depth and epicentral-distance sorting of waveforms.
5. Equidistant plotting of waveforms in seismic sections.

The waveform processing was further supported by the particle motion analysis to recognize the type of the secondary phases. In addition, the secondary phases were numerically modeled by considering several alternative structure models.

The analysis revealed prominent secondary phases at most recordings of all three studied stations. The secondary phases exhibit a constant time delay after the direct *P* wave arrivals, though this value varies among stations. Detail analysis performed for high-quality recordings at station GOK shows that the major secondary phase is detected at ~0.9 s after the direct *P* wave onset independently of the location and depth of the earthquakes. The polarization of this secondary phase is consistent with that of the direct *S* wave, which suggests that the major secondary phase is the *PS* conversion. Some clusters exhibit also a minor secondary phase detected at ~0.5 s after the *P* wave onsets, but it is less consistent within the clusters and has smaller amplitudes. Its polarization is vertical and suggests a *P*-type phase.

The origin of the major secondary *PS* phase was numerically tested with synthetic modeling. Since the time delay of this phase does not change substantially for the analyzed clusters, it should be generated at a structure near or below the stations. Figure 13a presents a schematic sketch with the horizontal interface producing the *PS* phase. Figure 13b presents a schematic sketch with a steeply inclined reflecting/converting

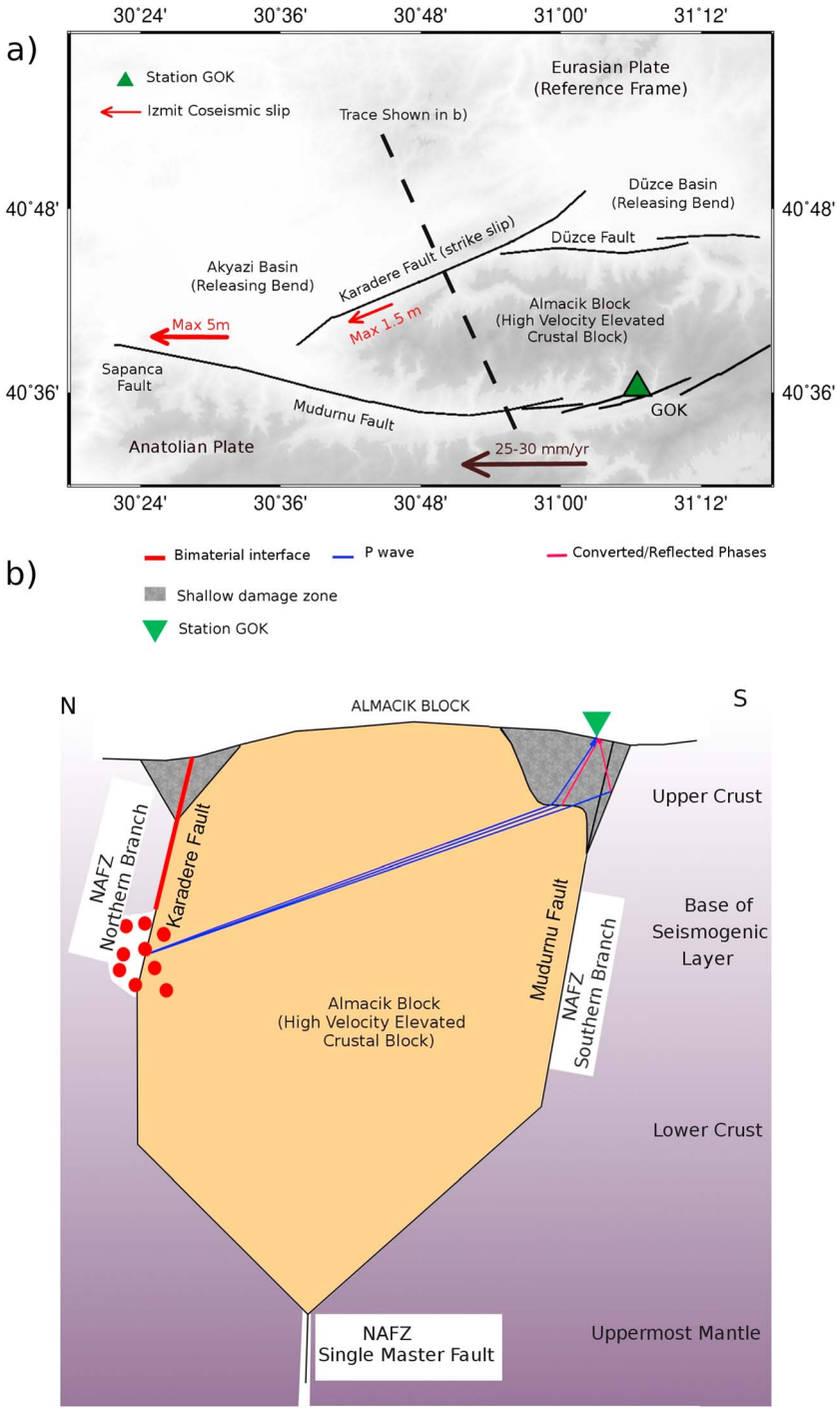

Figure 14. Conceptual model in (a) map and (b) fault-normal views. (a) The red arrows show values of the maximum İzmit coseismic slip. The black arrow shows the horizontal velocity of the Anatolian Plate with respect to the Eurasian Plate in the north. (b) The Almacik block is colored in yellow. The gray area north of the Almacik block at the Karadere fault represents a shallow low-velocity zone or damaged basin; the red line represents the deep bimaterial interface detected by Najdahmadi et al. (2016). The gray area south of the Almacik block at the Mudurnu fault shows a similar structure trapped between two hard blocks where the secondary phases interpreted in this study were produced. The red circles represent the earthquakes; the blue lines represent the rays for direct waves; the pink lines represent rays for reflected and converted waves observed in this study.

interface (or fault zone) producing both major *PS* reflected conversions and minor *PP* reflections. Unfortunately, the analysis of the particle motions of the major secondary phases does not help us to further discriminate between the two models. Because of anisotropy in the upper crust both direct and converted *S* phases are affected by shear-wave splitting, which poses limitations on the interface identification. In addition, the minor *P*-type secondary phase is noisy and it is difficult to resolve whether it is produced by the horizontally layered or steeply inclined structure. Nevertheless, the variation in its polarization suggests that the phase is rather reflected from an inclined interface than converted from a horizontal structure.

The time delay of ~0.9 s detected at station GOK is fitted by a velocity model with a steeply inclined interface reflecting the geological setting of the Mudurnu fault zone with a higher velocity at its southern side as observed further to the west (Bulut, Ben-Zion, et al., 2012). Such a model produces the *PS* conversions with a roughly constant time delay after the *P* wave arrival. Since this model also predicts the *PP* reflections preceding the *PS* phase generated at the same interface, it represents the most robust interpretation of the systematically observed secondary phases.

Alternatively, a horizontal interface at a depth of 4 km with the downward increasing velocities can be considered since models with horizontal layers are quite common in crustal studies (e.g., Hrubcová et al., 2016; Kennett et al., 1995). In such a case, a horizontal structure producing converted *PS* phases with a certain time delay after the direct *P* wave should also produce converted *SP* phases with similar time delay before the *S* wave arrivals. However, such a phase is systematically missing in the studied recordings from different azimuths. Furthermore, the secondary phases generated at a horizontal interface should come with the same time delay at all studied stations. However, the time delays of the secondary phases differ in the recordings of stations DOK and EKI, which also disfavors the model with one horizontal interface for all three stations.

To conclude, a steep Mudurnu fault zone as the origin of the *PS* reflected conversions at shallow depths of ~2–3 km is the most plausible explanation of the *PS* conversions systematically observed in the seismic waveforms. However, since the waveforms are complicated, its effect can be enhanced by the proximity of a horizontal interface at ~4 km depth. Najdahmadi et al. (2016) reported fault zone head waves with a constant time delay prior to the direct *P* arrivals along the Karadere fault. This observation was interpreted with a shallow low-velocity zone or an evolving pull-apart basin structure (see Figure 14) related to a progression of the two transtensional features at either end of the Karadere fault, the Akyazi Basin in the SW, and the Düzce Basin in the NE (Figure 14a). Our interpretation of the secondary phases with a constant time delay after the direct *P* wave arrivals could be another manifestation of such a juvenile and evolving early stage of a pull-apart structure at the southern side of the Almacik block, the Mudurnu fault, which would be in good agreement with the regional transtensional setting (see Figure 14b). However, in fact, both such structures can be present along the Mudurnu fault generating fault-related phases as discussed by Li et al. (2007) and Yang et al. (2011). The high-quality recordings at station GOK compared to less pronounced secondary phases detected at stations EKI and DOC point to a strong steeply inclined or near vertical fault structure with stations located at different sides of the fault and the station GOK in the optimum position in front of the Mudurnu fault in respect to the analyzed seismicity.

In our study, we focused on the recordings at station GOK located in front of the Mudurnu fault. Application of the method to data recorded at the stations DOK and EKI located in a vicinity of this fault may help to disclose the complex structure of the Mudurnu area. Above, the technique applied here may serve to image the near-vertical faults in other areas and determine potential hazard-prone faults thereby contributing to better constrain future rupture planes.

Acknowledgments
The work was supported by the Grant Agency of the Czech Republic grants 17-19297S and 16-19751J, and by funding from the German Research Foundation DFG under the project Bo1877-8. We thank Amir Allam for providing the code for quantified polarization analysis. The authors are grateful to the Editor Yehuda Ben-Zion, Associate Editor, and two anonymous reviewers for their valuable comments. The analyzed waveforms are available from ftp://ftp.gfz-potsdam.de/home/georg/Imaging-Mudurnu-Segment-Najdahmadi-etal/Data/.

References

Allam, A. A., & Ben-Zion, Y. (2012). Seismic velocity structures in the southern California plate-boundary environment from double-difference tomography. *Geophysical Journal International*, *190*(2), 1181–1196. https://doi.org/10.1111/j.1365-246X.2012.05544.x

Ambraseys, N. N., & Zatopek, A. (1969). The Mudurnu Valley, West Anatolia, Turkey, earthquake of 22 July 1967. *Bulletin of the Seismological Society of America*, *59*(2), 521–589.

Barka, A., Akyüz, H., Altunel, E., Sunal, G., Cakir, Z., Dikbas, A., … Page, W. (2002). The surface rupture and slip distribution of the 17 August 1999 İzmit earthquake (*M*7.4), North Anatolian fault. *Bulletin of the Seismological Society of America*, *92*(1), 43–60. https://doi.org/10.1785/0120000841

Barka, A. A. (1992). The North Anatolian fault zone. *Annales Tectonicae, Special Issue VI* (pp. 164–195). Firenze, Italy: Annales tectonicae : International journal of structural geology and tectonics.

Beyhan, G., & Alkan, M. A. (2015). Three-dimensional structure of Vp in the upper crust of the Sakarya Basin, NW Turkey. *Arabian Journal of Geosciences*, *8*(8), 6371–6383. https://doi.org/10.1007/s12517-014-1605-6

Bindi, D., Parolai, S., Görgün, E., Grosser, H., Milkereit, C., Bohnhoff, M., & Durukal, E. (2007). ML scale in northwestern Turkey from 1999 İzmit aftershocks: Updates. *Bulletin of the Seismological Society of America*, *97*(1B), 331–338. https://doi.org/10.1785/0120060071

Bohnhoff, M., Grosser, H., & Dresen, G. (2006). Strain partitioning and stress rotation at the North Anatolian fault zone from aftershock focal mechanisms of the 1999 İzmit M_w = 7.4 earthquake. *Geophysical Journal International*, *166*(1), 373–385. https://doi.org/10.1111/j.1365-246X.2006.03027.x

Bohnhoff, M., Harjes, H.-P., & Meier, T. (2005). Deformation and stress regimes in the Hellenic subduction zone from focal mechanisms. *Journal of Seismology*, *9*(3), 341–366. https://doi.org/10.1007/s10950-005-8720-5

Bohnhoff, M., Ickrath, M., & Dresen, G. (2016). Seismicity distribution in conjunction with spatiotemporal variations of coseismic slip and postseismic creep along the combined 1999 İzmit-Düzce rupture. *Tectonophysics*, *686*, 132–145. https://doi.org/10.1016/j.tecto.2016.07.029

Bohnhoff, M., Martínez-Garzón, P., Bulut, F., Stierle, E., & Ben-Zion, Y. (2016). Maximum earthquake magnitudes along different sections of the North Anatolian fault zone. *Tectonophysics*, *674*, 147–165. https://doi.org/10.1016/j.tecto.2016.02.028

Bouchon, M. (1981). A simple method to calculate Green's functions for elastic layered media. *Bulletin of the Seismological Society of America*, *71*(4), 959–971.

Brückl, E., Bleibinhaus, F., Gosar, A., Grad, M., Guterch, A., Hrubcová, P., … Thybo, H. (2007). Crustal structure due to collisional and escape tectonics in the Eastern Alps region based on profiles Alp01 and Alp02 fromthe ALP 2002 seismic experiment. *Journal of Geophysical Research*, *112*, B06308. https://doi.org/10.1029/2006JB004687

Bulut, F., Ben-Zion, Y., & Bohnhoff, M. (2012). Evidence for a bimaterial interface along the Mudurnu segment of the North Anatolian Fault Zone from polarization analysis of P waves. *Earth and Planetary Science Letters*, *34*(20), 17–22. https://doi.org/10.1029/2007GL031154

Bulut, F., Bohnhoff, M., Aktar, M., & Dresen, G. (2007). Characterization of aftershock fault plane orientations of the 1999 İzmit (Turkey) earthquake using high-resolution aftershock locations. *Geophysical Research Letters*, *34*, L20306. https://doi.org/10.1029/2007GL031154

Bulut, F., Bohnhoff, M., Eken, T., Janssen, C., Kilic, T., & Dresen, G. (2012). The East Anatolian Fault Zone: Seismotectonic setting and spatio-temporal characteristics of seismicity based on precise earthquake locations. *Journal of Geophysical Research*, *117*, B07304. https://doi.org/10.1029/2011JB008966

Červený, V., & Pšenčík, I. (1984). SEIS83 – Numerical modeling of seismic wave fields in 2-D laterally varying layered structures by the ray method. In E. R. Engdal (Ed.), *Documentation of Earthquake Algorithms*, *Rep. SE-35* (pp. 36–40). Boulder, CO: World Data Center A for Solid Earth Geophysics.

Dor, O., Yildirim, C., Rockwell, T. K., Ben-Zion, Y., Emre, O., Sisk, M., & Duman, T. Y. (2008). Geological and geomorphologic asymmetry across the rupture zones of the 1943 and 1944 earthquakes on the North Anatolian Fault: Possible signals for preferred earthquake propagation direction. *Geophysical Journal International*, *173*(2), 483–504. https://doi.org/10.1111/j.1365-246X.2008.03709.x

Eberhart-Phillips, D., & Michael, A. J. (1993). Three-dimensional velocity structure, seismicity, and fault structure in the Parkfield region, central California. *Journal of Geophysical Research*, *98*, 15,737–15,758. https://doi.org/10.1029/93JB01029

Eken, T., Bohnhoff, M., Bulut, F., Can, B., & Aktar, M. (2013). Crustal anisotropy in the Eastern Sea of Marmara region in northwestern Turkey. *Bulletin of the Seismological Society of America*, *103*(2A), 911–924. https://doi.org/10.1785/0120120156

Flerit, F., Armijo, R., King, G., & Meyer, B. (2004). The mechanical interaction between the propagating North Anatolian Fault and the back-arc extension in the Aegean. *Earth and Planetary Science Letters*, *224*(3-4), 347–362. https://doi.org/10.1016/j.epsl.2004.05.028

Görgün, E., Bohnhoff, M., Bulut, F., & Dresen, G. (2010). Seismotectonic setting of the Karadere–Düzce branch of the North Anatolian Fault Zone between the 1999 İzmit and Düzce ruptures from analysis of İzmit aftershock focal mechanisms. *Tectonophysics*, *482*(1-4), 170–181. https://doi.org/10.1016/j.tecto.2009.07.012

Gülen, L., Pinar, A., Kalafat, D., Ozel, N., Horasan, G., Yilmazer, M., & Isikara, A. M. (2002). Surface fault breaks, aftershock distribution, and rupture process of the 17 August 1999 İzmit, Turkey, earthquake. *Bulletin of the Seismological Society of America*, *92*(1), 230–244. https://doi.org/10.1785/0120000815

Hrubcová, P., Vavryčuk, V., Boušková, A., & Bohnhoff, M. (2016). Shallow crustal discontinuities inferred from waveforms of microearthquakes: Method and application to KTB Drill Site and West Bohemia Swarm Area. *Journal of Geophysical Research: Solid Earth*, *121*, 881–902. https://doi.org/10.1002/2015JB012548

Hrubcová, P., Vavryčuk, V., Boušková, A., & Horálek, J. (2013). Moho depth determination from waveforms of microearthquakes in the West Bohemia/Vogtland swarm area. *Journal of Geophysical Research: Solid Earth*, *118*, 120–137. https://doi.org/10.1029/2012JB009360

Hurd, O., & Bohnhoff, M. (2012). Stress- and structure-induced shear-wave anisotropy along the 1999 İzmit rupture, Northwest Turkey. *Bulletin of the Seismological Society of America*, *102*(5), 2177–2188. https://doi.org/10.1785/0120110270

Ickrath, M., Bohnhoff, M., Bulut, F., & Dresen, G. (2014). Stress rotation and recovery in conjunction with the 1999 Izmit M_w 7.4 earthquake. *Geophysical Journal International*, *196*(2), 951–956. https://doi.org/10.1093/gji/ggt409

Ickrath, M., Bohnhoff, M., Dresen, G., Martínez-Garzón, P., Bulut, F., Kwiatek, G., & Germer, O. (2015). Detailed analysis of spatiotemporal variations of the stress field orientation along the İzmit-Düzce rupture in NW Turkey from inversion of first-motion polarity data. *Geophysical Journal International*, *202*(3), 2120–2132. https://doi.org/10.1093/gji/ggv273

Jurkevics, A. (1988). Polarization analysis of three-component array data. *Bulletin of the Seismological Society of America*, *78*(5), 1725–1743.

Kaiser, A. E., Green, A. G., Campbell, F. M., Horstmeyer, H., Manukyan, E., Langridge, R. M., … Nobes, D. C. (2009). Ultrahigh-resolution seismic reflection imaging of the Alpine Fault, New Zealand. *Journal of Geophysical Research*, *114*, B11306. https://doi.org/10.1029/2009JB006338

Kennett, B. L. N., Engdahl, E. R., & Buland, R. (1995). Constraints on seismic velocities in the Earth from travel times. *Geophysical Journal International*, *122*(1), 108–124. https://doi.org/10.1111/j.1365-246X.1995.tb03540.x

Li, H., Zhu, L., & Yang, H. (2007). High-resolution structures of the landers fault zone inferred from aftershock waveform data. *Geophysical Journal International*, *171*(3), 1295–1307. https://doi.org/10.1111/j.1365-246X.2007.03608.x

Li, X., Cormier, V. F., & Toksöz, M. N. (2002). Complex source process of the 17 August 1999 İzmit, Turkey, earthquake. *Bulletin of the Seismological Society of America*, *92*(1), 267–277. https://doi.org/10.1785/0120000839

McClusky, S., Balassanian, S., Barka, A., Demir, C., Ergintav, S., Georgiev, I., … Kahle, H. (2000). Global Positioning System constraints on plate kinematics and dynamics in the eastern Mediterranean and Caucasus. *Journal of Geophysical Research*, *105*, 5695–5719. https://doi.org/10.1029/1999JB900351

Milkereit, C., Zünbül, S., Karakisa, S., Iravul, Y., Zschau, J., Baumbach, M., … Karahan, A. (2000). Preliminary aftershock analysis of the M_w = 7.4 İzmit and M_w = 7.1 Düzce earthquake in Western Turkey. In Ö. Kozaci & A. Barka (Eds.), *The 1999 İzmit and Düzce Earthquakes: Preliminary results* (pp. 179–187). Istanbul, Turkey: Istanbul Technical University.

Najdahmadi, B., Bohnhoff, M., & Ben-Zion, Y. (2016). Bimaterial interfaces at the Karadere segment of the North Anatolian Fault, northwestern Turkey. *Journal of Geophysical Research: Solid Earth*, *121*, 931–950. https://doi.org/10.1002/2015JB012601

Örgülü, G., & Aktar, M. (2001). Regional moment tensor inversion for strong aftershocks of the August 17, 1999 İzmit earthquake (M_w = 7.4). *Geophysical Research Letters*, *28*, 371–374. https://doi.org/10.1029/2000GL011991

Özalaybey, S., Ergin, M., Aktar, M., Tapirdamaz, C., Biçmen, F., & Yörük, A. (2002). The 1999 Izmit earthquake sequence in Turkey: Seismological and tectonic aspects. *Bulletin of the Seismological Society of America*, *92*(1), 376–386.

Papaleo, E., Cornwell, D. G., & Rawlinson, N. (2017). Seismic tomography of the North Anatolian Fault: New insights into structural heterogeneity along a continental strike-slip fault. *Geophysical Research Letters*, *44*, 2186–2193. https://doi.org/10.1002/2017GL072726

Peng, Z., & Ben-Zion, Y. (2004). Systematic analysis of crustal anisotropy along the Karadere-Düzce branch of the North Anatolian fault. *Geophysical Journal International*, *159*(1), 253–274. https://doi.org/10.1111/j.1365-246X.2004.02379.x

Sanford, A. R., Alptekin, O., & Toppozada, T. R. (1973). Use of reflection phases on microearthquake seismograms to map unusual discontinuity beneath the Rio Grande rift. *Bulletin of the Seismological Society of America*, *63*(6), 2021–2034.

Sengör, A., Tüysüz, O., Imren, C., Sakinç, M., Eyidogan, H., Görür, N., … Rangin, C. (2005). The North Anatolian fault: A new look. *Annual Review of Earth and Planetary Sciences*, *33*(1), 37–112. https://doi.org/10.1146/annurev.earth.32.101802.120415

Stierle, E., Bohnhoff, M., & Vavryčuk, V. (2014). Resolution of non-double-couple components in the seismic moment tensor using regional networks-II: Application to aftershocks of the 1999 M_w 7.4 İzmit earthquake. *Geophysical Journal International*, *196*(3), 1878–1888. https://doi.org/10.1093/gji/ggt503

Stierle, E., Vavryčuk, V., Šílený, J., & Bohnhoff, M. (2014). Resolution of non-double-couple components in the seismic moment tensor using regional networks-I: A synthetic case study. *Geophysical Journal International*, *196*(3), 1869–1877. https://doi.org/10.1093/gji/ggt502

Thybo, H., Janik, T., Omelchenko, V., Grad, M., Garetsky, R., Belinsky, A., … Sand, R. (2003). Upper lithospheric seismic velocity structure across the Pripyat Trough and the Ukrainian Shield along the EUROBRIDGE'97 profile. *Tectonophysics*, *371*(1-4), 41–79. https://doi.org/10.1016/S0040-1951(03)00200-2

Tibi, R., Bock, G., Xia, Y., Baumbach, M., Grosser, H., Milkereit, C., … Zschau, J. (2001). Rupture processes of the 1999 August 17 İzmit and November 12 Düzce (Turkey) earthquakes. *Geophysical Journal International*, *144*(2), F1–F7. https://doi.org/10.1046/j.1365-246x.2001.00360.x

Vavryčuk, V., Hrubcová, P., Brož, M., & Málek, J. (2004). Azimuthal variation of Pg velocity in the Moldanubian, Czech Republic: Observations based on a multi-azimuthal common-shot experiment. *Tectonophysics*, *387*(1-4), 189–203. https://doi.org/10.1016/j.tecto.2004.06.015

Waldhauser, F., & Ellsworth, W. L. (2000). A double-difference earthquake location algorithm: Method and application to the northern Hayward fault, California. *Bulletin of the Seismological Society of America*, *90*(6), 1353–1368. https://doi.org/10.1785/0120000006

Wu, H., & Lees, J. M. (1999). Three-dimensional P and S wave velocity structures of the Coso geothermal area, California, from microseismic travel time data. *Journal of Geophysical Research*, *104*, 13,217–13,233. https://doi.org/10.1029/1998JB900101

Yang, H. (2015). Recent advances in imaging crustal fault zones: A review. *Earthquake Science*, *28*(2), 151–162. https://doi.org/10.1007/s11589-015-0114-3

Yang, H., Zhu, L., & Cochran, E. S. (2011). Seismic structures of the Calico fault zone inferred from local earthquake travel time modelling. *Geophysical Journal International*, *186*(2), 760–770. https://doi.org/10.1111/j.1365-246X.2011.05055.x